

Non-destructive Evaluation of the Contribution of Polymer-Fibre Orientation and Distribution Characteristics to Concrete Performance during Fire



Tyler Oesch, Ludwig Stelzner and Frank Weise

Abstract Although concrete itself is not a combustible material, concrete mixtures with high density, such as high-performance concretes (HPCs), are susceptible to significant damage during fires due to explosive spalling. Past research has shown that the inclusion of polymer fibres in high density concrete can significantly mitigate this fire damage. The exact mechanisms causing this increased spalling resistance are not yet fully understood, but it is thought that the fibres facilitate moisture transport during fire exposure, which in turn contributes to relief of internal stresses in the spalling-susceptible region. In this study, X-ray Computed Tomography (CT) was applied to observe the interaction between polymer fibres and cracking during thermal exposure. For this purpose, two concrete samples containing different polymer fibre types were subjected to incremental application of a defined thermal exposure. CT images were acquired before and after each thermal exposure and powerful image processing tools were used to segment the various material components. This enabled a detailed analysis of crack formation and propagation as well as the visualization and quantification of polymer fibre characteristics within the concrete. The results demonstrated that the orientation of both fibres and cracks in polymer-fibre reinforced concrete tend to be anisotropic. The results also indicated that crack geometry characteristics may be correlated with fibre orientation, with cracks tending to run parallel to fibre beds. Clear quantitative relationships were also observed between heating and increasing cracking levels, expressed in terms of both crack surface area and crack volume.

T. Oesch (✉) · L. Stelzner · F. Weise
Bundesanstalt für Materialforschung und –prüfung,
Federal Institute for Materials Research and Testing, 12205 Berlin, Germany
e-mail: tyler.oesch@bam.de

L. Stelzner
e-mail: ludwig.stelzner@bam.de

F. Weise
e-mail: frank.weise@bam.de

© Springer Nature Switzerland AG 2019
H. Herrmann and J. Schnell (eds.), *Short Fibre Reinforced Cementitious
Composites and Ceramics*, Advanced Structured Materials 95,
https://doi.org/10.1007/978-3-030-00868-0_4

1 Introduction

1.1 Performance of Concrete During Fire

Although concrete itself is not a combustible material, concrete structural components are susceptible to explosive spalling during fire. The investigation and control of this phenomenon is very important since the spalling of individual components can have a significant effect on the overall fire resistance of structures. Structural fire resistance, in turn, has major implications both to the safety of first responders during fires as well as the costs associated with structural repair following a fire.

It has been demonstrated that this spalling behaviour is at least partially related to the presence of moisture within the concrete material [9, 28]. Spalling behaviour is also increased for high-strength concretes (HSCs), which generally possess a higher overall density and lower permeability [7, 27]. The increase in the popularity and use of these high-strength concretes in building construction heightens the urgency of developing better methods for predicting and mitigating the effects of this spalling behaviour [1].

Fibre-reinforced concretes have been used in building construction since at least the 1970s [30]. Fibres have generally been used in these concrete mixes to improve the ductility and durability of the material [13, 33]. Polymer fibres have also been shown, however, to significantly contribute to spall resistance within concrete components during fire [8, 9].

The exact mechanisms causing this increased spalling resistance are not yet fully understood, but it is thought that the fibres facilitate moisture transport during fire exposure, which in turn contributes to relief of internal stresses in the spalling-susceptible region [9, 25]. The formation of a fibre-induced micro-cracking network has been identified as one important aspect of this process [25]. At the present time, there is also no comprehensive understanding of how fibre properties, such as polymer type, diameter, length, shape, and density, affect overall spalling performance of concrete members during fire. Optimization of these parameters will need to be completed before polymer-fibre reinforced concretes are adopted into widespread use for fire protection.

1.2 X-Ray Computed Tomography

X-ray computed tomography (CT) has been used in non-destructive concrete research applications for more than 30 years [15, 19]. In this scanning method, a sample is placed on a rotating table between an X-ray source and an X-ray detector [4]. This causes an X-ray attenuation image of the sample to be projected upon the detector. By recording these projected images during the 360° rotation of the sample, mathematically-based reconstruction algorithms can be used to produce a three dimensional representation of X-ray attenuation within the sample [3]. The X-ray

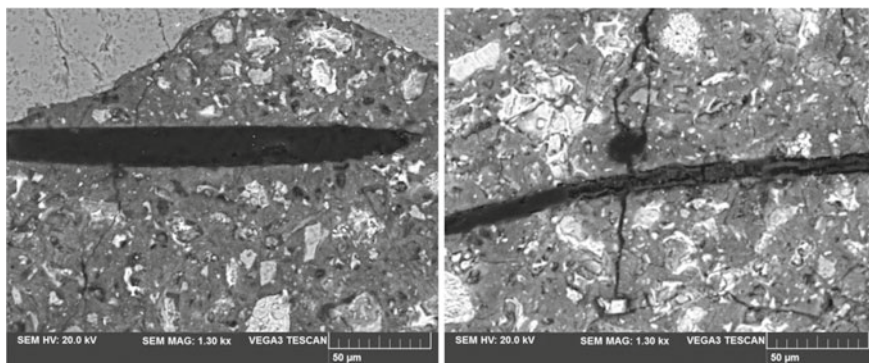


Fig. 1 Scanning Electron Microscope (SEM) images of polymer fibres before (left) and after (right) heating to 300 °C

attenuation, which is roughly correlated with density, of individual component materials within the sample can then be identified and objects made from these component materials can be individually separated and analysed.

1.3 Objectives and Significance

Previous research has shown that small cracks develop in the mortar that surrounds the fibres during curing (Fig. 1). One goal of this research was to investigate to what extent these curing cracks contribute to overall material permeability prior to and during heating.

Another goal of this research was to identify the presence of correlations between fibre and cracking orientation characteristics and to quantitatively define the strength of those correlations. Previous research has demonstrated that the fibre fields in FRCs tend to be highly anisotropic because of flow during the casting process [5, 6, 17, 18, 20–22, 26]. It is thought that this anisotropy could have a major effect on fire resistance and, if properly controlled, may serve as a means of significantly improving spalling resistance.

The third goal of this research was to quantitatively measure the crack growth during incremental heating through the use of X-ray computed tomography (CT). This CT-based data would be particularly well suited for the calibration and validation of computational models of the spalling phenomenon.

2 Materials and Sample Preparation

The investigated specimens were made of HSC and were reinforced with different amounts and types of polypropylene (PP) fibres (Table 1). The mixture HSC / PPa2 contained 2 kg/m³ conventional PP-fibres. In contrast, for HSC / PPb1 only 1 kg/m³ pre-treated PP-fibres was added. The PPb-fibres were pre-treated during the manufacturing process using electron irradiation. This leads to a decreased fibre-melt viscosity [24] and improves the fire performance of the concrete, despite the reduced amount of added PP-fibres.

Initially, cubes (100 × 100 × 100 mm³) were cast for both mixtures. After demoulding on the next day, these cubes were stored under water for six days and subsequently in a climate chamber at 20 °C and 65 % relative humidity for a minimum of 83 days. Subsequently, cylindrical specimens with diameters of 12 mm and lengths of 100 mm were extracted from the cubes. A single cylindrical sample from each of the two cubes was selected for heating and CT analysis. These two samples will henceforward be referred to as sample PPb1 and sample PPa2, in reference to their composition. Before the first CT-measurement was carried out, these cylinders were fixed firmly within a customized set of mobile clamps, which ensured consistent mounting positions during repetitive CT measurements.

Table 1 HSC mixture

Component			Content [kg/m ³] in concrete type	
			HSC / PPa-2	HSC / PPb-1
Cement CEM 42,5 R			580	
Water (w/c = 0,33)			173	
Aggregate (quarzitic)	0/2	[mm]	744	
	2/4		223	
	4/8		521	
Silica fume			63,8	
Superplasticizer			27,8	
PP-fibre type (∅ 15,4 µm, L = 6 mm)		a	2	-
		b	-	1

Where:

PPa = conventional polypropylene fibres

PPb = pre-treated polypropylene fibres

3 Test Methods

After preparing and mounting the concrete cylinders, a CT-measurement was completed. Thereby, the initial structure of the concrete was analysed. Afterwards, the clamped concrete cylinders were heated using a special heating regime to reach specific maximum temperatures (see Thermal Loading). Subsequent to each heating/cooling phase, a further CT-measurement was carried out to investigate the crack formation in the fibre-reinforced HSC as a result of the thermal exposure.

3.1 Thermal Loading

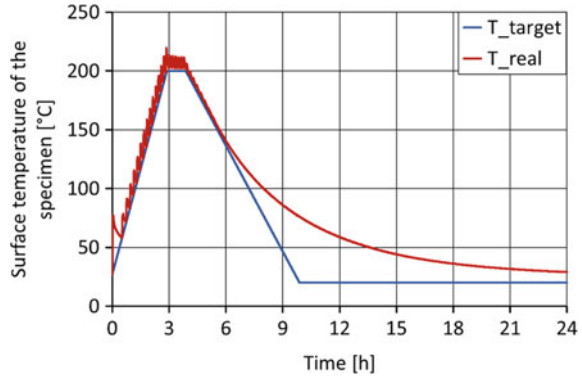
During the test series, the specimens were heated to certain target temperatures (150, 160, 170, 180, 190, 200, 250, 300 °C) using an electrical furnace (Fig. 2). During thermal testing, the heat was increased at a rate of 1 K/min until the respective target temperature was reached. The target temperature was then sustained for one hour, followed by cooling at a maximum rate of $-0,5$ K/min to room temperature prior to CT-scanning.

The used electrical furnace is controlled by a temperature controller. The oven temperature is determined on the basis of the temperature measurement of a thermocouple, which is fixed in the rear wall of the furnace. Figure 3 shows an example temperature curve measured with an additional installed thermocouple near the



Fig. 2 Electrical furnace containing a typical clamped specimen

Fig. 3 Example temperature curve for heating test at 200 °C



specimen in comparison with the target temperature curve. Thereby it can be seen that the temperature in the furnace is controlled very well during heating phase. During the cooling phase the actual cooling rate is slower than the prescribed one because of the nonlinearity of the natural cooling process.

3.2 CT Scanning

During this research program, an acceleration voltage of 60 kV and current of 130 μ A were used for the X-ray source. The X-ray beam was also filtered using a 1 mm thick Aluminium plate immediately upon leaving the source in order to remove unwanted bandwidths from the X-ray beam and, in turn, make the resulting images more clear. The flat panel detector used for this scanning contained a 2048 \times 2048 pixel field. The resolution of the resulting CT images of the samples was 6.18 μ m.

4 Image Processing

4.1 Initial Processing Procedures

All image processing was completed using the program MATLAB [16]. The images were first corrected for beam hardening, which is a CT phenomenon causing the outer edges of the sample to appear brighter than its centre. During subsequent data analysis, it was found that the full sized sample image, which was 2048 \times 2048 \times 2048 voxels (a voxel is a 3D pixel), was much too large for the available image processing algorithms and computer system. Thus, a cubic sub-volume of 1200 \times 1200 \times 1200 voxels was digitally extracted from the centre of the original image and

used for all subsequent analysis. Through the use of this sub-volume, all resulting computational demands and run times were reduced by a factor of approximately five times.

To enable the density and orientation analysis of the fibres and cracks, these materials first needed to be identified and separated within the images. Although individual component materials can generally be separated within CT images using grayscale segmentation methods that was not sufficient for these sample images. The reason for this complication was that the X-ray attenuation levels of the air pores, the cracks, and the polymer fibres were found to all be very similar and partially overlapping. Thus, more complex methods of fibre and crack detection needed to be developed.

4.2 Fibre Identification

Initially, template matching methods were used in an attempt to identify the polymer fibres, but with only limited success. One reason for the failure of this method may have been that the fibres had such a small size within the images (only approximately 2.5 voxels in diameter) that their shape was not sufficiently well-defined to consistently match the template characteristics. Another problem with this method was that the polymer fibres often exhibited significant bending within the material, which made it even more difficult to define and match a consistent fibre shape.

To overcome these limitations, a customized multi-step approach was developed for fibre identification that exhibited considerable versatility and accuracy. The individual steps of this analysis procedure will be outlined in the description below:

Step 1. The triangle segmentation method [34, 35] was used to identify a boundary between low attenuation elements within the sample, including air pores, cracks, and polymer fibres, and high attenuation elements, including aggregate and mortar, on the voxel intensity histogram (Fig. 4). Using this attenuation threshold, a sample image containing only air pores, cracks, and fibres could be created and used for further analysis (Fig. 5).

Step 2. All objects within the low-attenuation image were individually analysed and those with a volume less than 16% of the standard individual fibre volume were removed from the image (Fig. 5). This was done in order to eliminate both noise and micro-pores from the image. The reason that some objects with less than 100% of the fibre volume were retained within the image was that, since the analysis was conducted upon a cubic sub-volume, many partial fibres existed along the image edge. It was desirable to retain these partial fibre segments for subsequent analysis steps as they were expected to contribute significantly to overall sample performance. The volume limitation of 16% was found through trial and error to produce a good balance between elimination of unwanted objects and retention of partial fibre segments.

Step 3. The objects within the image were contracted and then subsequently dilated by an amount equivalent to the fibre radius (rounded upward). This resulted in an image containing only objects larger in diameter than fibres. These macro-pores

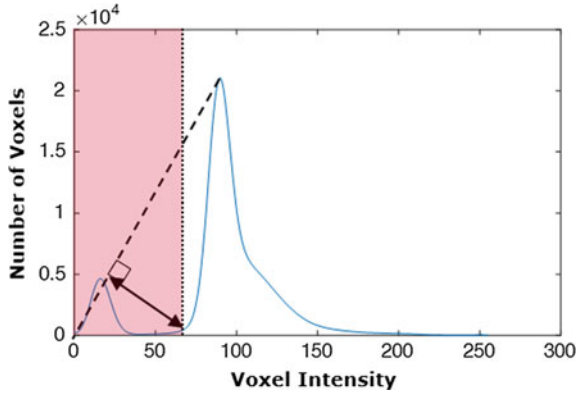


Fig. 4 Definition of low-high attenuation threshold on the voxel intensity histogram

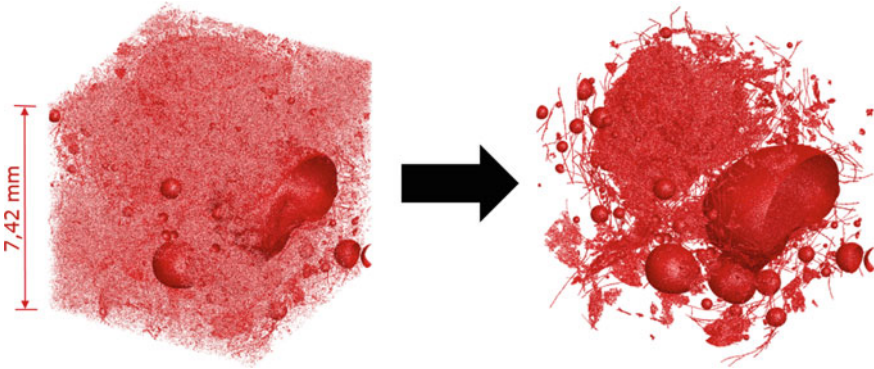


Fig. 5 Image of low-attenuation materials in sample PPb1 after step 1 (left) and step 2 (right)

were subsequently removed from the image produced by step 2 in order to reduce the number of non-fibre objects (Fig. 6).

Through the removal of all objects with diameter larger than and volume smaller than that of the fibres in steps 2 and 3, it was originally thought that a clear, fibre-only image would result. It was soon found, however, that the samples contained many small micro-cracks of width similar to the fibre diameter even prior to the application of heat. Closer inspection revealed that these micro-cracks were almost exclusively present within the aggregate, rather than the mortar.

Step 4. Since the fibres, in contrast to the cracks, are only present within the mortar, and never within aggregates, it was possible to develop an algorithm for separating the fibres from the remaining cracks. In this algorithm, each object was dilated by an amount equivalent to the fibre radius (rounded upward) and the attenuation of this dilated region was analysed. If the attenuation of the dilated region around an individual object corresponded to that representative of mortar (Figs. 7 and 8), the

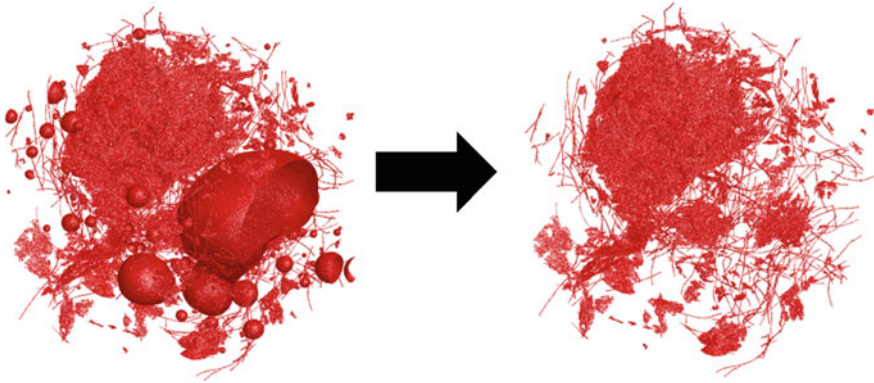


Fig. 6 Image of low-attenuation materials in sample PPb1 after step 2 (left) and after step 3 (right)

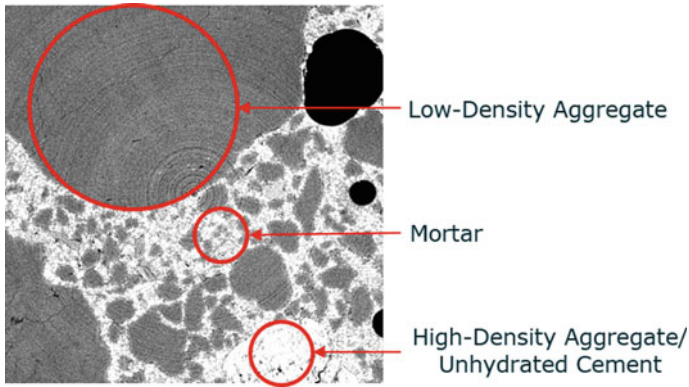


Fig. 7 Attenuation image of the fibre-reinforced concrete material visually demonstrating the attenuation differences between aggregate and mortar

object was considered a fibre and retained. All other objects were considered as micro-cracks within the aggregate and eliminated (Fig. 9).

The resulting fibre images for samples PPb1 and PPa2 can be compared in Fig. 10. Although these images still contain some non-fibre objects, the overall contribution of these objects to the measured fibre characteristics is assumed to be small. These non-fibre objects are thought to primarily consist of cracks or small voids that intersect with fibres as well as ring artefacts.

As previously described, the sample PPa2 was fabricated to contain a fibre volume twice that of sample PPb1. The differences in fibre volume between the analysed sub-volumes of the two samples shown in Fig. 10, however, exhibit a much larger volume difference. The fibre volume percentage within each analysed sub-volume could be calculated by summing the number of voxels of fibre material and dividing that number by the total number of voxels in the image. Using this method a fibre-

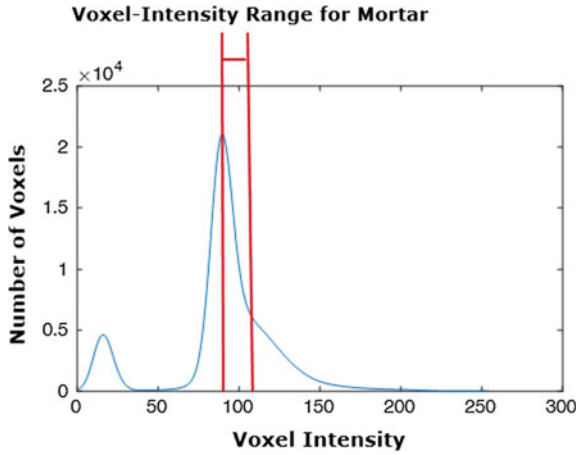


Fig. 8 Definition of attenuation threshold boundaries for mortar material on the voxel intensity histogram

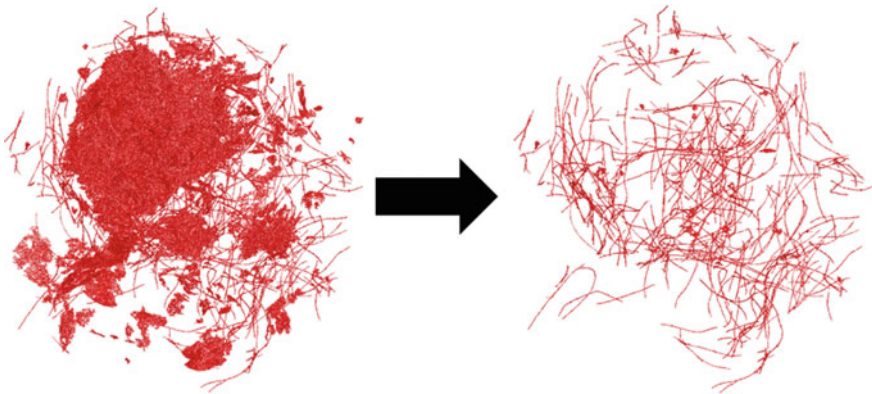


Fig. 9 Image of low-attenuation materials in sample PPb1 after step 3 (left) and after step 4 (right)

volume percentage of 0.202% was measured for the PPa2 sub-volume, which was very close to the 0.22% fibre-volume percentage used in the mix design.

For the PPb1 sub-volume, however, a fibre-volume percentage of only 0.044% was measured as opposed to the 0.11% fibre-volume percentage used in the mix design. There are many possible reasons for such a discrepancy. The most likely causes are inhomogeneity of fibre distribution within the sample and the presence of large aggregates or air-voids within the sub-volume selected for analysis. Both of these sources of error would be significantly reduced through the selection of larger sub-volumes for analysis. There is, thus, an impetus for further development of these image processing algorithms in order to reduce their computational requirements and enable the analysis of larger sub-volumes in future scanning and analysis efforts.

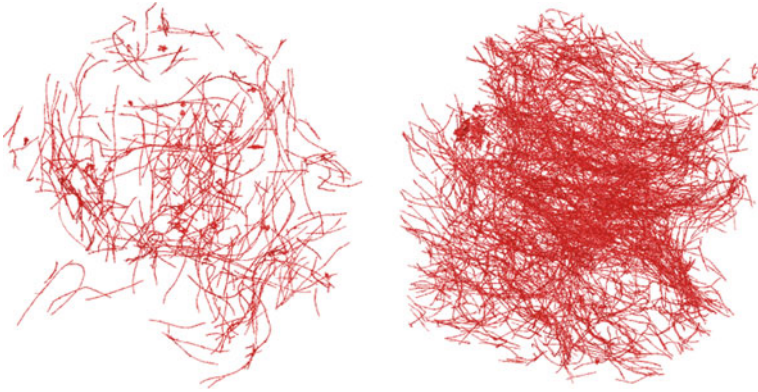


Fig. 10 Fibre images for samples PPb1 (left) and PPa2 (right)

4.3 Fibre Analysis

Once the fibres had been identified and isolated within the images, they were then analysed for both density and orientation characteristics. The orientation analysis was completed using the Hessian-based method [6, 14]. In this method, the grayscale images resulting from CT are considered to be three-dimensional functions that are twice differentiable in all directions [10]. By calculating the Hessian matrix at a given voxel within a fibre, partial second derivatives can be computed:

$$H = \begin{bmatrix} \frac{\partial^2 I}{\partial x^2} & \frac{\partial^2 I}{\partial x \partial y} & \frac{\partial^2 I}{\partial x \partial z} \\ \frac{\partial^2 I}{\partial y \partial x} & \frac{\partial^2 I}{\partial y^2} & \frac{\partial^2 I}{\partial y \partial z} \\ \frac{\partial^2 I}{\partial z \partial x} & \frac{\partial^2 I}{\partial z \partial y} & \frac{\partial^2 I}{\partial z^2} \end{bmatrix} \quad (1)$$

with H = Hessian Matrix and I = Grayscale Sample Image Matrix.

At this point, the second derivative in the direction of the longitudinal axis of the fibre will be much less than those in the transverse directions. The orientation of fibres can, thus, be assessed by computing the eigenvalues and eigenvectors of the Hessian matrix at each voxel within a fibre (Fig. 11). The primary fibre orientation recorded at a single fibre voxel, therefore, is the eigenvector corresponding to the smallest eigenvalue [29].

For the fibre density analysis method, a small cell size was selected, comprising a cube with 120 voxel (742 μm) long sides. The fibre image was broken up into an array of these cells, and the number of white (i.e., fibre) voxels in each was counted. By dividing the number of fibre voxels in each cell by the total number of cell voxels, estimates of local fibre density within the sample could be obtained.

The cell size used for the density analysis was selected such that the length of each cube side represented about a 10th of the overall length of a typical image array side.

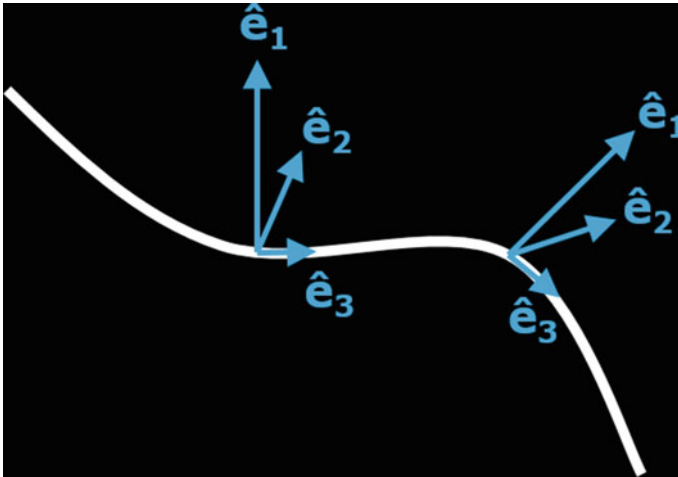


Fig. 11 Eigenvectors of the Hessian matrix at two points within a fibre

This meant that a sufficient number of cells (1000) would be available for analysis to enable meaningful statistical evaluation. This is because for a pseudo-random phenomenon, such as fibre density variation, a large number of samples need to be collected to observe meaningful trends within the statistical data. At the same time, however, there was a desire to avoid cell sizes that were too small because they might be too highly influenced by the presence of single fibres.

4.4 Cracking Analysis

The lack of a consistent size or shape for the crack geometry also made template matching techniques of limited use for crack identification. These characteristics made the use of a customized isolation approach similar to that used for the fibres unsuitable as well.

Past research has demonstrated, however, that many cracking characteristics can be measured through the observation of changes in void properties in images of progressively damaged samples [21, 23]. In this approach, all void characteristics, including volume, surface area, and orientation, within the initial, undamaged scan of a sample are assumed to be related to entrained and entrapped air. Thus, any change in these void characteristics, such as volume and surface area growth, seen in later scans of damaged samples can be assumed to be due to cracking and, thus, represented as crack characteristics.

It is important to note, however, that when analysing the orientation of cracks, a modified version of the approach used for fibre orientation analysis must be applied. Since cracks are planar objects, they cannot be characterized by a single, parallel

vector in the way that fibres can. Rather, the cracks must be characterised by a vector which is perpendicular to the plane of the crack. Thus, in the Hessian characterization of crack orientation, the orientation angle represented by the eigenvector corresponding to the largest eigenvalue of the Hessian matrix must be used.

5 Results and Discussion

5.1 Results of Fibre Analysis

Various methods exist to depict and analyse orientation data in three dimensions. For the present analysis, coordinates have been converted from a Cartesian to a spherical system [32]:

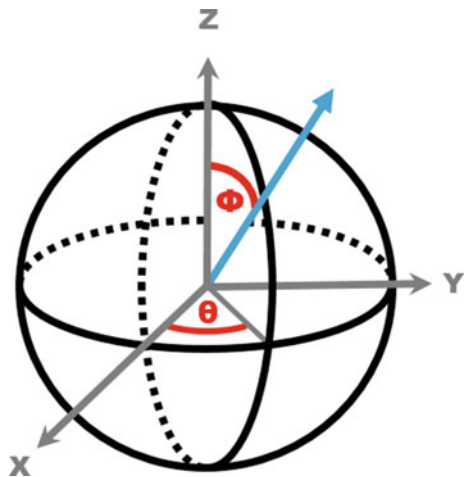
$$r = \sqrt{x^2 + y^2 + z^2} , \tag{2}$$

$$\theta = \tan^{-1} \left(\frac{y}{x} \right) , \tag{3}$$

$$\phi = \cos^{-1} \left(\frac{z}{r} \right) . \tag{4}$$

In this spherical coordinate system, orientations are characterized by angles θ and ϕ (Fig. 12). The angle θ represents the azimuthal angle in the x-y plane from the x-axis (in this context the cylindrical axis of the sample is denoted as the z-axis), with $0 < \theta < 360^\circ$ (Eq. 3). The angle ϕ represents the polar angle from the positive z-axis. Since the fibres are fully symmetric, a symmetry condition is likewise imposed on ϕ , with $0 < \phi < 90^\circ$ (Eq. 4).

Fig. 12 Spherical coordinate system



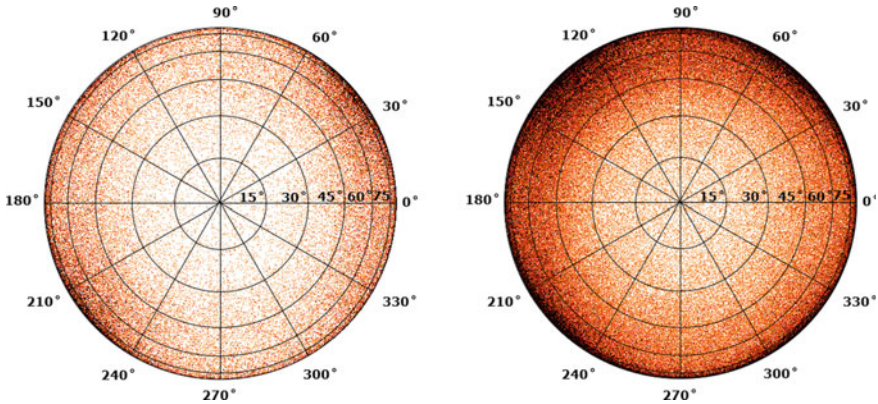


Fig. 13 Orthogonal projections of fibre orientation for samples PPb1 (left) and PPa2 (right). Projection radius: $0 < \phi < 90^\circ$; projection circumference: $0 < \theta < 360^\circ$

Figure 13 provides orthogonal projections of the fibre orientation data for samples PPb1 and PPa2. The depiction of three-dimensional data on a two-dimensional plane makes these projections unsuitable for evaluating isotropy along the ϕ -axis but the projections can be used very effectively for evaluating isotropy along the θ -axis. For sample PPb1, there appeared to be an anisotropic orientation of fibres along roughly the $\theta = 30^\circ/210^\circ$ axis. A similar, although less clear anisotropy also appeared in the projection for sample PPa2. The darker colours of the PPa2 projection were caused by the higher fibre-volume content already discussed.

Fibre density results can be displayed in the form of histograms (Figs. 14 and 15). For clarity, the y-axis in these histograms has been depicted in logarithmic scale. This is necessary since the vast majority of cubic sub-volumes contain no fibres or only a few fibre voxels. These histograms confirm the higher fibre-volume content of sample PPa2.

5.2 Results of Cracking Analysis

The void data were also analysed using spherical coordinates and changes in void orientation characteristics, which correspond to crack orientation characteristics, can be depicted using orthogonal projections (Fig. 16).

Recalling that the crack orientations were measured in terms of orientation normal to the cracking plane, it can be observed that for both PPb1 and PPa2, there appears to be an anisotropy along roughly the $\theta = 130^\circ/310^\circ$ plane. This indicates that the primary orientation of the cracks is parallel to the primary fibre orientation. This is because the primary normal orientation of the cracks (depicted in Fig. 16) is roughly orthogonal to the primary fibre orientation (depicted in Fig. 13), which is typical for a plane running parallel to a line.

Fig. 14 Histogram of fibre density for sample PPb1

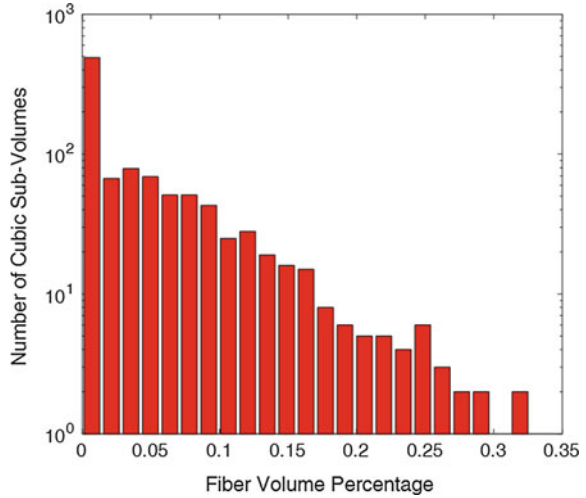
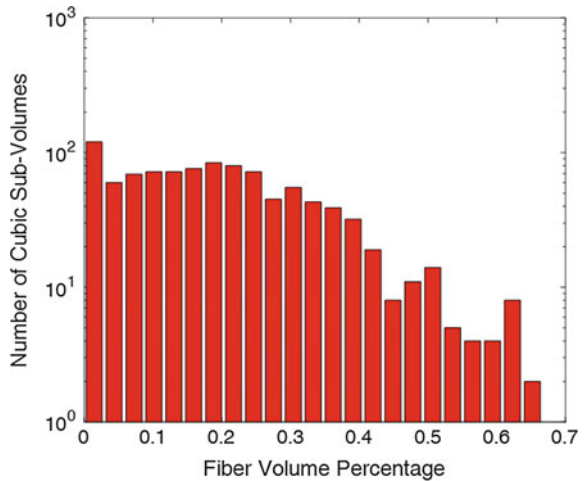


Fig. 15 Histogram of fibre density for sample PPa2



5.3 Comparison of Fibre and Cracking Characteristics

Comparison of fibre and cracking characteristics based purely on Figs. 13 and 16 is rather qualitative and difficult, however. In order to provide a more amenable means for direct comparison, histograms of fibre and crack-normal orientation were created and overlaid (Figs. 17 and 18).

The relationship between the θ -orientations of the fibres and the normal vectors to the cracking plane for PPb1 exhibit behaviour typical of cracks running along the primary fibre orientation direction, with very few fibres oriented along the directions normal to the cracking plane. This correlation is less clear for the PPa2 data.

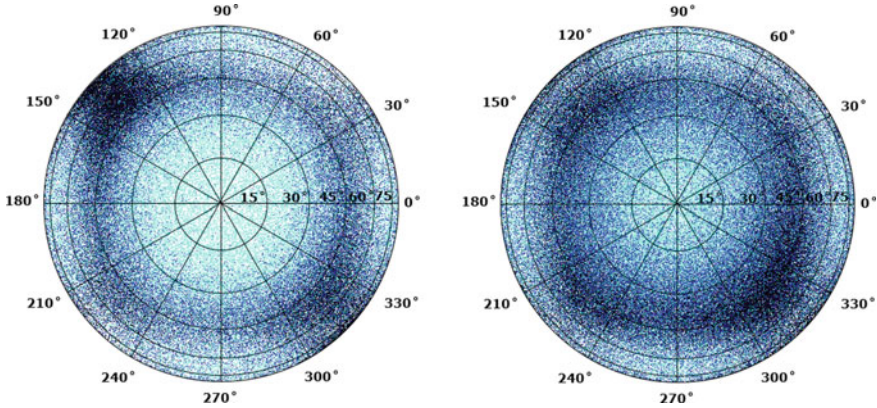
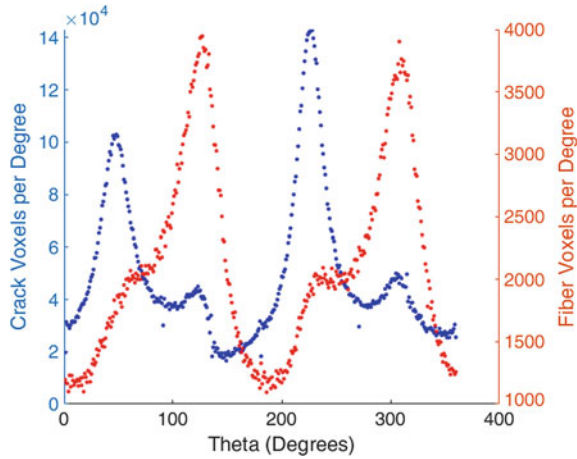


Fig. 16 Orthogonal projections of the normal orientation vectors measured for the cracks in samples PPb1 (left) and PPa2 (right) after 300°C heating. Projection radius: $0 < \phi < 90^\circ$; projection circumference: $0 < \theta < 360^\circ$

Fig. 17 Relationship between fibre (red) and crack-normal (blue) θ -orientation for sample PPb1



The reasons for this are unclear, but may be related to the higher volume of fibres contained within this sample. This increase in fibre volume may lead to more concerted behaviour of fibres through their combination in bundles as opposed to the less dense fibres in PPb1, which are more likely to interact with the concrete material individually. The presence of crack or ring artefacts within the fibre images could also contribute to this inconsistency.

Fibre-cracking histograms have also been created relative to the ϕ -orientation (Figs. 19 and 20). Direct evaluation of these histograms is complicated by the fact that fibre density is not uniform along the ϕ -axis due to exponential growth of volume in the unit sphere corresponding with linear increases in ϕ -angle. Very similar trends in ϕ -orientation are observable for the fibre and crack-normal data of both samples

Fig. 18 Relationship between fibre (red) and crack-normal (blue) θ -orientation for sample PPa2

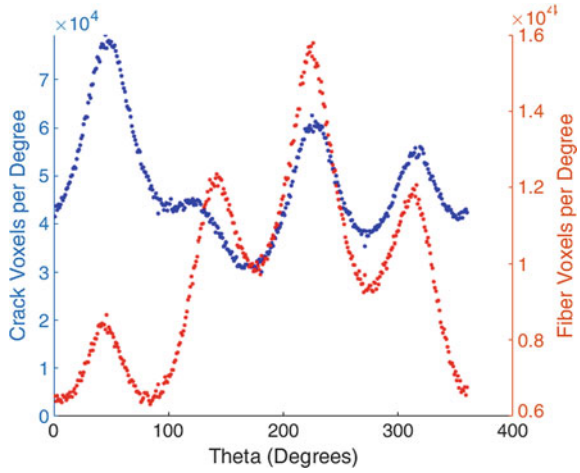
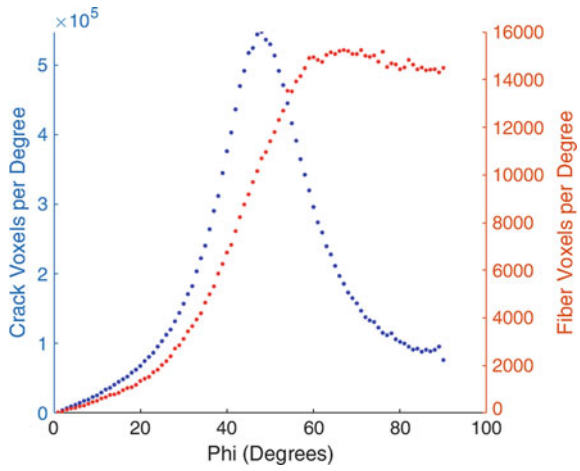


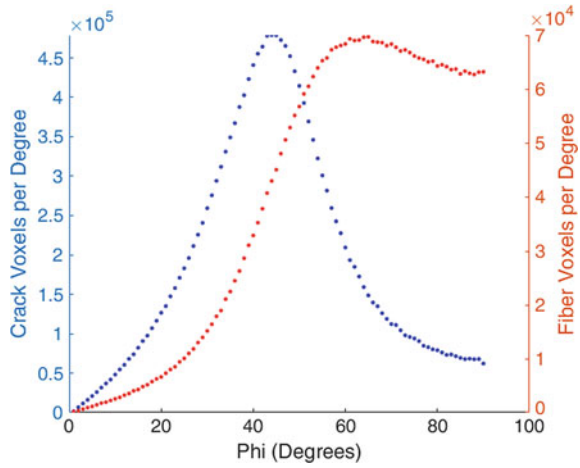
Fig. 19 Relationship between fibre (red) and crack-normal (blue) ϕ -orientation for sample PPb1



PPb1 and PPa2. These figures provide confirmation that an offset between the fibre and crack-normal orientation exists. Although not clearly orthogonal to one another, as would be expected for perfectly parallel cracks and fibres, this orientation offset does indicate that the cracks tend to orient themselves more strongly parallel to fibres than perpendicular to them.

A detailed analysis of fiber-crack interactions within localized regions of these samples can also be found in [31].

Fig. 20 Relationship between fibre (red) and crack-normal (blue) ϕ -orientation for sample PPa2



5.4 Correlation between Heating and Cracking Characteristics

Much clearer trends can be observed in the growth of cracking relative to temperature increase. Figures 21, 22, 23 and 24 depict the growth of cracking relative to applied heating for both samples PPb1 and PPa2. In these figures, two different measurements are used to evaluate cracking growth. Figures 21 and 22 are plotted relative to crack volume while Figs. 23 and 24 are plotted relative to crack surface area.

Fig. 21 Relationship between temperature and crack volume for sample PPb1

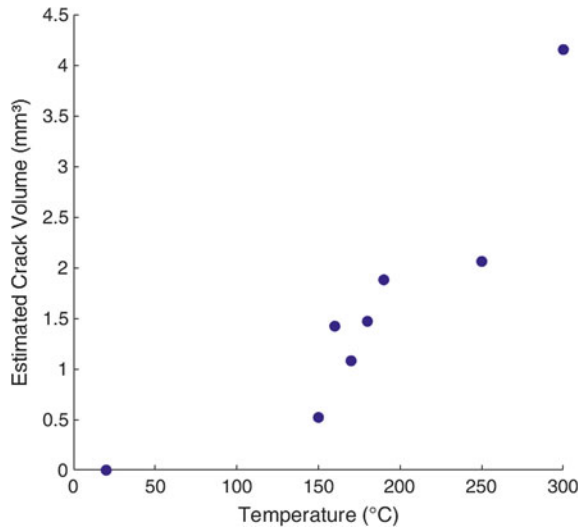


Fig. 22 Relationship between temperature and crack volume for sample PPa2

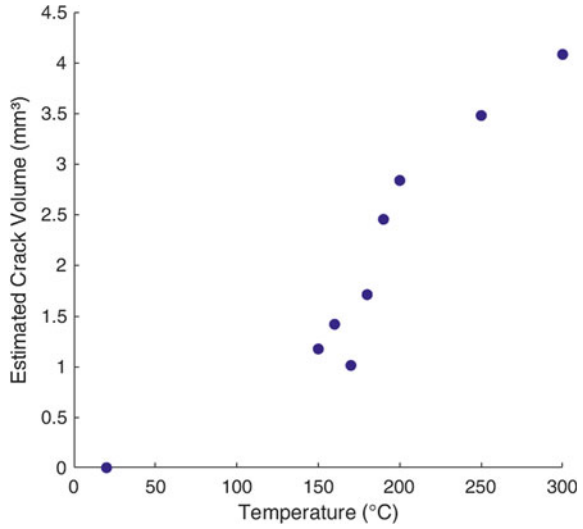
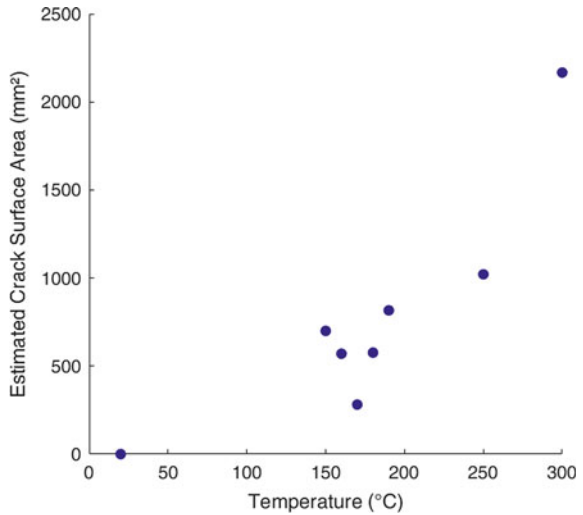
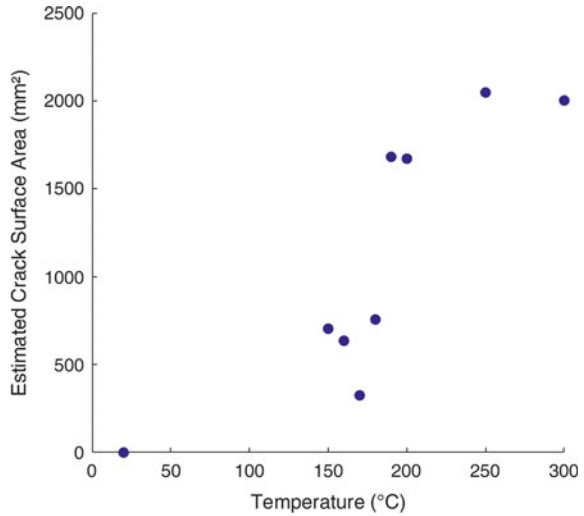


Fig. 23 Relationship between temperature and crack surface area for sample PPb1



In each of these figures, clear trends are visible between cracking and heating characteristics. These quantitative trends offer great promise for the calibration and validation of fire-damage models within finite element analysis codes for concrete. Basic fracture mechanics uses crack surface area as one parameter for calculating fracture energy [2]. This may make crack surface area the optimal damage parameter for use in numerical modelling.

Fig. 24 Relationship between temperature and crack surface area for sample PPa2



Crack volumes have, however, also previously been shown to follow clear trends relative to work-of-load and stiffness reduction [11, 12]. The optimal numerical approach might be to develop a calibration and validation approach that combines the measurements of both of these cracking characteristics.

6 Conclusions

The results of this research effort have demonstrated that the orientation of both fibres and cracks in polymer-fibre reinforced concrete tend to be anisotropic. It is thought that this anisotropy is predominantly influenced by casting method, but can also be affected by the presence of large aggregates or voids within the sample. The results of the orientation analysis also indicated that crack geometry characteristics may be correlated with fibre orientation, with cracks tending to run parallel to fibre beds. This could have major implications for structural level performance since it would indicate that fire resistance may be related to casting method.

Clear quantitative relationships were also observed between heating and increasing cracking levels, expressed in terms of both crack surface area and crack volume. These relationships can serve as the basis for calibration and validation of finite element models used for simulating heat-related spalling behaviour.

7 Future Work

Future research is needed both to improve the accuracy and reliability of the analysis procedures used in this research and to develop new analysis procedures for evaluating phenomena of relevance to the spalling behaviour of concrete. One reason that only aggregated cracking and fibre characteristics could be measured in this research was the lack of accurate digital volume correlation (DVC) tools. The development and application of such tools would enable direct comparison, including subtraction, of individual image features among multiple images in a heating or loading series. This would not only make it easier to distinguish crack growth and fibre failure, but it would also enable more accurate measurements of crack-fibre property correlation. Up to the present time it has been very difficult to develop accurate DVC tools for concrete analysis because of the cracking discontinuities typical of concrete failure, which are generally more difficult for DVC methods to accommodate than the simple strains typical of plastically deforming materials.

New methods also need to be developed for assessing the cross-linking of fibre beds during heat-related cracking. Although this phenomenon has been observed using SEM, it has been difficult to develop a method that accurately quantifies the material behaviour. This is further complicated by the fact that many of the connecting cracks observed during SEM scanning appear to be below the resolution of most laboratory CT systems. It is believed that significant progress could be made in measuring this phenomenon through the skilled application of synchrotron-CT scanning in combination with DVC image processing tools.

Finally, further development of the image processing algorithms detailed in this paper is needed. These algorithms should be streamlined to enable orientation analysis of larger regions of interest within samples, which would minimize the magnitude of error introduced by individual material features, such as single stones or voids. Further research is also needed to improve the precision of the fibre-cracking orientation comparison and to statistically quantify the correlation level. Only through the accurate measurement of statistical correlation between fibre and cracking orientation can firm conclusions be drawn about the optimal casting procedures for the construction of fire-resistant building components.

References

1. Aitcin, P.C.: High Performance Concrete. CRC Press (1998). <https://doi.org/10.1201/9781420022636>
2. Bazant, Z.P., Planas, J.: Fracture and Size Effect in Concrete and Other Quasibrittle Materials, vol. 16. CRC Press (1997)
3. Feldkamp, L.A., Davis, L.C., Kress, J.W.: Practical cone-beam algorithm. *J. Opt. Soc. Am. A* **1**(6), 612–619 (1984). <https://doi.org/10.1364/JOSAA.1.000612>
4. Flannery, B.P., Deckman, H.W., Roberge, W.G., D'Amico, K.L.: Three-dimensional x-ray microtomography. *Science* **237**(4821), 1439–1444 (1987). <https://doi.org/10.1126/science.237.4821.1439>

5. Herrmann, H., Lees, A.: On the influence of the rheological boundary conditions on the fibre orientations in the production of steel fibre reinforced concrete elements. *Proc. Est. Acad. Sci.* **65**(4), 408–413 (2016). <https://doi.org/10.3176/proc.2016.4.08.Open-AccessCC-BY-NC4.0>
6. Herrmann, H., Pastorelli, E., Kallonen, A., Suuronen, J.P.: Methods for fibre orientation analysis of x-ray tomography images of steel fibre reinforced concrete (SFRC). *J. Mater. Sci.* **51**(8), 3772–3783 (2016). <https://doi.org/10.1007/s10853-015-9695-4>
7. Hertz, K.: Explosion of silica-fume concrete. *Fire Saf. J.* **8**(1), 77 (1984). [https://doi.org/10.1016/0379-7112\(84\)90057-2](https://doi.org/10.1016/0379-7112(84)90057-2)
8. Jansson, R.: Material Properties Related to Fire Spalling of Concrete. Division of Building Materials. Lund Institute of Technology, Lund University (2008)
9. Jansson, R.: Fire spalling of concrete: theoretical and experimental studies. Ph.D. thesis, KTH Royal Institute of Technology (2013)
10. Krause, M., Hausherr, J.M., Burgeth, B., Herrmann, C., Krenkel, W.: Determination of the fibre orientation in composites using the structure tensor and local x-ray transform. *J. Mater. Sci.* **45**(4), 888 (2010). <https://doi.org/10.1007/s10853-009-4016-4>
11. Landis, E.N.: Toward a physical damage variable for concrete. *J. Eng. Mech.* **132**(7), 771–774 (2006). [https://doi.org/10.1061/\(ASCE\)0733-9399\(2006\)132:7\(771\)](https://doi.org/10.1061/(ASCE)0733-9399(2006)132:7(771))
12. Landis, E.N., Zhang, T., Nagy, E.N., Nagy, G., Franklin, W.R.: Cracking, damage and fracture in four dimensions. *Mater. Struct.* **40**(4), 357–364 (2007). <https://doi.org/10.1617/s11527-006-9145-5>
13. Li, V.C., Wang, S.: Microstructure variability and macroscopic composite properties of high performance fiber reinforced cementitious composites. *Probab. Eng. Mech.* **21**(3), 201–206 (2006). <https://doi.org/10.1016/j.probengech.2005.10.008> (Probability and Materials: from Nano- to Macro-Scale)
14. Lorenz, C., Carlsen, I.C., Buzug, T.M., Fassnacht, C., Weese, J.: Multi-scale line segmentation with automatic estimation of width, contrast and tangential direction in 2D and 3D medical images. In: *CVRMed-MRCAS'97*, pp. 233–242. Springer (1997)
15. Martz, H.E., Scheberk, D.J., Roberson, G.P., Monteiro, P.J.: Computerized tomography analysis of reinforced concrete. *Mater. J.* **90**(3), 259–264 (1993)
16. Mathworks T: Matlab. r2014a. Natick, MA, USA (2016)
17. Mishurova, T., Léonard, F., Oesch, T., Meinel, D., Bruno, G., Rachmatulin, N., Fontana, P., Sevostianov, I.: Evaluation of fiber orientation in a composite and its effect on material behavior. In: *Proceedings of the 7th Conference on Industrial Computed Tomography (ICT) held February 7–9, 2017, Leuven, Belgium*, vol. 22(03). NDT.net (2017). <http://www.ndt.net/?id=20818>
18. Mishurova, T., Rachmatulin, N., Fontana, P., Oesch, T., Bruno, G., Radi, E., Sevostianov, I.: Evaluation of the probability density of inhomogeneous fiber orientations by computed tomography and its application to the calculation of the effective properties of a fiber-reinforced composite. *Int. J. Eng. Sci.* **122**, 14–29 (2018). <https://doi.org/10.1016/j.jengsci.2017.10.002>
19. Morgan, I., Ellinger, H., Klinksiek, R., Thompson, J.N.: Examination of concrete by computerized tomography. *J. Proc.* **77**(1), 23–27 (1980)
20. Oesch, T., Landis, E., Kuchma, D.: A methodology for quantifying the impact of casting procedure on anisotropy in fiber-reinforced concrete using x-ray ct. *Mater. Struct.* **51**(3), Article 73, 1–13 (2018). <https://doi.org/10.1617/s11527-018-1198-8>
21. Oesch, T.S.: Investigation of fiber and cracking behavior for conventional and ultra-high performance concretes using x-ray computed tomography. University of Illinois at Urbana-Champaign (2015)
22. Oesch, T.S.: In-situ ct investigation of pull-out failure for reinforcing bars embedded in conventional and high-performance concretes. In: *Proceedings of 6th Conference on Industrial Computed Tomography (ICT)*, vol. 21 (2016)
23. Oesch, T.S., Landis, E.N., Kuchma, D.A.: Conventional concrete and UHPC performance–damage relationships identified using computed tomography. *J. Eng. Mech.* **142**(12), 04016101 (2016)
24. Pistol, K.: Wirkungsweise von polypropylen-fasern in brandbeanspruchtem hochleistungs-beton. doctoralthesis, Bundesanstalt für Materialforschung und -prüfung (BAM) (2016)

25. Pistol, K., Weise, F., Meng, B., Schneider, U.: The mode of action of polypropylene fibres in high performance concrete at high temperatures. In: 2nd International RILEM Workshop on Concrete Spalling due to Fire Exposure, pp. 289–296. RILEM Publications SARL (2011)
26. Pujadas, P., Blanco, A., Cavalaro, S., de la Fuente, A., Aguado, A.: Fibre distribution in macro-plastic fibre reinforced concrete slab-panels. *Constr. Build. Mater.* **64**, 496–503 (2014)
27. Sanjayan, G., Stocks, L.: Spalling of high-strength silica fume concrete in fire. *Mater. J.* **90**(2), 170–173 (1993)
28. Stelzner, L., Powierza, B., Weise, F., Oesch, T.S., Dlugosch, R., Meng, B.: Analysis of moisture transport in unilateral-heated dense high-strength concrete. In: Proceedings from the 5th International Workshop on Concrete Spalling, pp. 227–239 (2017)
29. Trainor, K.: 3-D analysis of energy dissipation mechanisms in steel fiber reinforced reactive powder concrete. Master's thesis, The University of Main (2011)
30. Urbana-Champaign UoIa: The history of concrete: a timeline. Department of Materials Science and Engineering. <http://matse1.matse.illinois.edu/concrete/hist.html> (2015)
31. Weise, F., Stelzner, L., Weinberger, J., Oesch, T.S.: Influence of the pre-treatment of pp-fibres by means of electron irradiation on the spalling behaviour of high strength concrete. In: Proceedings from the 5th International Workshop on Concrete Spalling, pp. 345–358 (2017)
32. Weisstein, E.W.: Spherical Coordinates. From MathWorld—A Wolfram Web Resource (2017). <http://mathworld.wolfram.com/SphericalCoordinates.html>
33. Williams, E.M., Graham, S.S., Reed, P.A., Rushing, T.S.: Laboratory characterization of cor-tuf concrete with and without steel fibers. Tech. rep, Engineer Research and Development Center Vicksburg MS Geotechnical and Structures Lab (2009)
34. Young, I.T., Gerbrands, J.J., Van Vliet, L.J.: Fundamentals of Image Processing. Delft University of Technology Delft (1998)
35. Zack, G., Rogers, W., Latt, S.: Automatic measurement of sister chromatid exchange frequency. *J. Histochem. Cytochem.* **25**(7), 741–753 (1977)